AGU PUBLICATIONS

JGR

Journal of Geophysical Research: Solid Earth

RESEARCH ARTICLE

10.1002/2014JB011454

This article is a companion to *Drombosky and Hier-Majumder* [2015], doi:10.1002/2014JB011068.
doi:10.1002/2014JB011454.

Key Points:
- Shear wave anisotropy with deformation
- 3% shear wave anisotropy by melt films
- LAB contains <1 vol % horizontal melt films

Correspondence to:
S. Hier-Majumder,
Saswata.Hier-Majumder@rhul.ac.uk

Citation:
Hier-Majumder, S., and T. Drombosky (2015), Development of anisotropic contiguity in deforming partially molten aggregates: 2. Implications for the lithosphere-asthenosphere boundary, *J. Geophys. Res. Solid Earth*, *120*, 764–777, doi:10.1002/2014JB011454.

Received 11 JUL 2014
Accepted 13 DEC 2014
Accepted article online 19 DEC 2014
Published online 3 FEB 2015

Development of anisotropic contiguity in deforming partially molten aggregates: 2. Implications for the lithosphere-asthenosphere boundary

Saswata Hier-Majumder[1] and Tyler Drombosky[2]

[1]Department of Earth Sciences, Royal Holloway University of London, Egham, UK, [2]Applied Math, Statistics, and Scientific Computation, University of Maryland, College Park, Maryland, USA

Abstract In this article, we calculate the seismic anisotropy resulting from melt redistribution during pure and simple shear deformation. Deformation strongly modifies the geometry of melts initially occupying three grain junctions. The initially isotropic fractional area of intergranular contact, contiguity, becomes anisotropic due to deformation. Consequently, the component of contiguity evaluated on the plane parallel to axis of maximum compressive stress decreases. During both modes of deformation, the trace of the contiguity tensor remains nearly unchanged. In the companion article [labeled DHM], we outline the numerical methods and present the synthetic micrographs from our numerical deformation experiments. In pure shear deformation, the principal contiguity directions remain stationary while they rotate during simple shear. The ratio between the principal components of the contiguity tensor decrease from 1 in an undeformed aggregate to 0.1 after 45% shortening in pure shear and to 0.3 after a shear strain of 0.75 in simple shear. In both pure and simple shear experiments, anisotropy in the shear wave velocity increases with the strain in a strongly nonlinear fashion. In pure shear deformation, the steady state microstructure produces nearly 3% anisotropy between shear waves vibrating perpendicular and parallel to the planes of melt films.

1. Introduction

Deformation of partially molten aggregates plays an important role in grain scale redistribution of melt. After deformation, the initially isotropic network of grain edge tubules becomes anisotropic as the melt preferentially wets grain boundaries oriented parallel to the principal compressive stress [*Daines and Kohlstedt*, 1997; *Takei*, 2005]. Such a transformation of the microstructure of the melt also renders contiguity, the fractional area of intergranular contact, anisotropic. As the elastic strength of the aggregate depends on the area of contact between adjacent, load-bearing grains, development of anisotropy in contiguity renders the effective elastic strength anisotropic, even if the solid matrix is isotropic.

Direct observation of the evolution of anisotropy of contiguity and shear wave speed during the course of deformation was previously precluded by the set-up of laboratory experiments and prohibitive computational cost of numerical models. Here, we present the results from a Fast Multipole Boundary Elements Method (FMBEM) based model that addresses the shortcomings of previous numerical models. In this work, we model the deformation of partially molten aggregates in pure and simple shear while tracking the information on shape and contiguity of each grain during each time step of the numerical experiment. In the companion article [*Drombosky and Hier-Majumder*, 2015, labeled DHM], we present the numerical methods and synthetic microstructures. In this article, we focus on the implications of our results on the Earth's Lithosphere-Asthenosphere Boundary (LAB).

The LAB is an ideal place to study the coupling between deformation and melt geometry. Results from experimental petrology indicate small amounts of melt, possibly less than 1 vol %, can exist in conditions similar to the LAB [*Sifré et al.*, 2014]. Dynamic coupling between the motion of lithospheric plates and the underlying asthenosphere will produce large amounts of deformation in the LAB, inducing strong anisotropy in the geometry of this melt [*Holtzman and Kendall*, 2010; *Kawakatsu et al.*, 2009]. The physical properties of this deformed, anisotropic aggregate should be able to explain the seismic and electric signature of the LAB.

Several constraints can be placed on the nature of the LAB from its seismic and electric signature. A number of studies indicate that despite regional variations, the LAB is characterized by a relatively sharp reduction in shear wave speed over a short depth range [*Schmerr*, 2012; *Fischer et al.*, 2010; *Rychert et al.*, 2010]. Another feature of the LAB is seismic anisotropy on global [*Nettles and Dziewoński*, 2008] and regional scales [*Holtzman and Kendall*, 2010]. Recent seismic observations by *Beghein et al.* [2014] indicate that the Gutenberg (G) discontinuity is marked by a sharp transition in seismic anisotropy and that G is distinct from the LAB. Magnetotelluric studies reveal that the LAB is characterized by a nearly horizontal channel of elevated electrical conductivity [*Evans et al.*, 2005; *Naif et al.*, 2013]. If partially molten, the interaction between deformation and redistribution of the melt should be able to explain these observed signatures of the LAB.

In this article, we explore the nature of the LAB from a microstructural perspective. In DHM, we demonstrate that the anisotropy in contiguity displays a strongly nonlinear increase as deformation progresses. In this article, we combine our results of anisotropic melt geometry with a mineral physics database using an averaging scheme to calculate the development of shear wave anisotropy during the course of deformation. We also compare the seismic signature of melt distributed in tubules with that of melt films created by grain boundary wetting.

This article is divided in the following sections. First we present the methods for calculating the contiguity, shear wave speeds, and anisotropy from our numerical data. Next, we discuss the evolution of the calculated seismic signature as a function of deformation. Finally, we discuss the implications of our study on the nature of seismic velocities, limitations of our work, and the nature of anisotropy in the LAB.

2. Methods

In this work, we use our numerical data to calculate the shear wave anisotropy. To estimate the effect of deformation in shear wave speed reduction and anisotropy generation, we also present predicted profiles of shear wave speed using the numerical code MuMaP [*Hier-Majumder et al.*, 2014]. In this section, we present a brief description of the numerical methods from DHM that were used to calculate the contiguity, followed by a derivation for calculating shear wave anisotropy from numerical values of contiguity, and a short summary of the technique used to build profiles of shear wave speed using MuMaP.

2.1. Numerical Model

In the microgeodynamic model of DHM, we carry out two sets of numerical experiments. In each set, the partially molten aggregate was modeled as a collection of two dimensional, tightly packed rounded hexagonal grains with an interstitial melt phase. During the deformation of this aggregate under an applied, constant strain rate, the grains and the melt deform in a viscous manner. We take the partial differential equations (PDEs) governing the conservation of mass and momentum within each grain and convert these PDEs into a Boundary Integral Equation (BIE) for each grain and melt phase. The vector BIE for the unknown velocity $\boldsymbol{u}^q(\boldsymbol{x}_0)$ at a point $\boldsymbol{x}_0$ on the boundary of the q^{th} grain is given by

$$\boldsymbol{u}^q(\boldsymbol{x}_0) = \frac{2}{1+\lambda_q}\left[\boldsymbol{u}^\infty(\boldsymbol{x}_0) - \frac{1}{4\pi Ca}\sum_P \int_{\Gamma_P} \Delta\boldsymbol{f}(\boldsymbol{x})\cdot\boldsymbol{\mathcal{U}}(\boldsymbol{x},\boldsymbol{x}_0)\,\mathrm{d}\Gamma_P + \sum_P \frac{1-\lambda_P}{4\pi}\int_{\Gamma_P}\boldsymbol{u}(\boldsymbol{x})\cdot\boldsymbol{\mathcal{T}}(\boldsymbol{x},\boldsymbol{x}_0)\cdot\hat{\boldsymbol{n}}\,\mathrm{d}\Gamma_P\right], \tag{1}$$

where λ_i is the ratio of viscosities between the i^{th} grain and the melt, $\boldsymbol{u}^\infty$ is an applied far-field velocity, $\Delta\boldsymbol{f}$ arises from tension at the surface of the grain, the second rank Stokeslet tensor $\boldsymbol{\mathcal{U}}$ arises from the response of the coupled flow within the grain and the melt to surface tension, the third rank Stresslet tensor $\boldsymbol{\mathcal{T}}$ arises from the contributions due to deformation within the grains, and $\hat{\boldsymbol{n}}$ is the unit normal vector along the boundary of the P^{th} grain, pointing into the melt. The interfacial tension term $\Delta\boldsymbol{f}$ in the first integral on the right-hand side is given by

$$\Delta\boldsymbol{f}(\boldsymbol{x}) = \gamma\hat{\boldsymbol{n}}\left(\boldsymbol{\nabla}\cdot\hat{\boldsymbol{n}}\right) \tag{2}$$

where γ is the surface tension and $\boldsymbol{\nabla}\cdot\hat{\boldsymbol{n}}$ is the spatially variable principal curvature at a point on the grain surface [*Leal*, 1992; *Pozrikidis*, 2001; *Kim and Karilla*, 2005; *Manga and Stone*, 1993]. The nondimensional capillary number Ca is the ratio between the forces of deformation and surface tension. In this analysis,

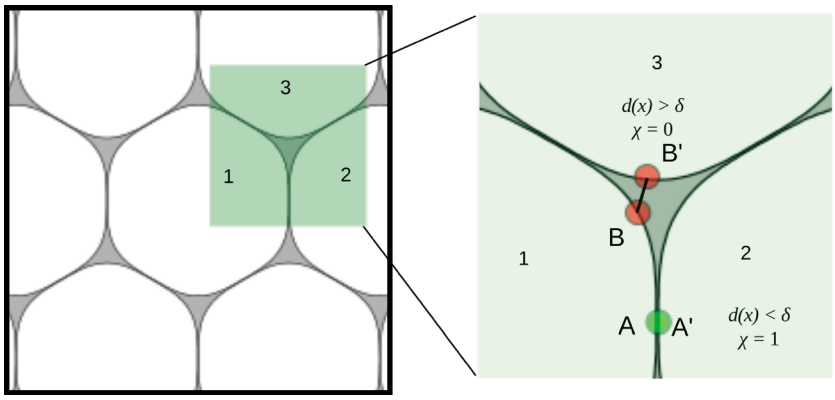

Figure 1. A schematic diagram outlining the calculation of contact function from simulated microstructures. The panel to the right represents an enlarged view of the shaded region in the left. A and B are two boundary nodes on the grain marked 1. A' and B' are boundary nodes on grains 2 and 3, respectively. For each of these boundary nodes, the Euclidean distance $d(x)$ is evaluated. The contact function for each boundary nodes is then calculated using equation (8). In this schematic diagram, the contact function is 1 for nodes A and A' but zero for boundary nodes B and B'.

we present results for $\lambda = 1$ and $Ca = 1$. For a detailed discussion on the BIE, we refer the reader to the companion article, DHM.

The shape of the P^{th} grain responds to the applied deformation. To ensure the volume of each grain is conserved, the shape function, F^P, evolves following the kinematic relation:

$$\frac{\partial F^P}{\partial t}(\boldsymbol{x}, t) + \boldsymbol{u}^P(\boldsymbol{x}, t) \cdot \nabla F^P = 0. \tag{3}$$

As the shape of the grain evolves, so does the contiguity. The contiguity tensor for the P^{th} grain at any time is given by

$$\boldsymbol{\psi}^P = \frac{1}{L} \int_{\Gamma_P} \chi(\boldsymbol{x}) \hat{\boldsymbol{n}}\hat{\boldsymbol{n}} \, \mathrm{d}\Gamma_P \tag{4}$$

where L is the length of Γ_P [*Takei*, 1998] and the unit normal, $\hat{\boldsymbol{n}}$, is numerically evaluated from F^P at each time step. The trace of the contiguity tensor, defined ψ (the tensorial quantity is written in boldface), is also numerically evaluated at each time step for each grain. The quantity $\chi(\boldsymbol{x})$ is the contact function [*Takei*, 1998], which assumes a value of unity at the grain-grain contact and zero at the grain melt contact.

To study the evolution of anisotropic contiguity by deformation, we carried out two sets of numerical experiments. In each set of experiment, the undeformed aggregate consists of a matrix packed with rounded hexagonal grains surrounded by six neighbors. Following *Hier-Majumder* [2008], the initial grain shape $F^{(P)}(0, \boldsymbol{x}) = 0$ is prescribed by the parametric representation,

$$\boldsymbol{x} = \begin{bmatrix} \cos(\theta) \\ \sin(\theta) \end{bmatrix} (1 - \epsilon \cos^2(3\theta)), \tag{5}$$

where θ is the counterclockwise angle from the positive x axis and the constant parameter $\epsilon = 0.05$ represents deviation of an individual grain shape from a unit circle [*Hier-Majumder*, 2008].

We carry out numerical experiments in pure shear and simple shear set up. In the numerical experiments, we want to simulate the response of the partially molten system under an applied, constant strain rate, $\dot{\mathbf{E}}$. This is achieved by prescribing the far-field velocity $\boldsymbol{u}^\infty = \dot{\mathbf{E}} \cdot \boldsymbol{x}$. For pure and simple shear experiments, the strain rate tensors $\dot{\mathbf{E}}_{\text{pure}}$ and $\dot{\mathbf{E}}_{\text{simple}}$ are defined as

$$\dot{\mathbf{E}}_{\text{pure}} = \begin{bmatrix} 1 & 0 \\ 0 & -1 \end{bmatrix}, \quad \text{and} \quad \dot{\mathbf{E}}_{\text{simple}} = \begin{bmatrix} 0 & 1 \\ 0 & 0 \end{bmatrix}. \tag{6}$$

For the pure shear experiments, the aggregate consisted of 1200 grains arranged in 40 rows and 30 columns, while the simple shear experiments were conducted on an aggregate of 900 grains arranged in 10 rows

and 90 columns. The detailed numerical methods are presented in DHM. For the seismic analysis in this article, we use the values of the components of the contiguity tensor, the eigenvalues, and the trace from the numerical experiment. We then average the values of these quantities over all grains at any given time step. These averaged values are then used to calculate the development of anisotropic contiguity and shear wave anisotropy as a function of increasing strain. The methods for calculation of contact functions and contiguity for each grain are outlined in the next section.

2.2. Determination of Contact Function and Contiguity

To evaluate contiguity of each grain, we first need to evaluate the contact function on the grain surface. The contact function χ is a step function, which assumes the value of unity at the grain-grain contact and zero at the grain-melt contact [*Takei*, 1998]. To calculate the contiguity of a grain, we need to know the unit normal vector and the value of contact function at each boundary node of each grain. At each time step of simulation, the normal vector at each boundary node is calculated from the known shape function (see DHM for details on the numerical techniques involved in calculating the grain geometry). To calculate the contact function at a boundary node of a grain, we use additional information on the position of all the boundary nodes of all neighboring grains, which is stored during each iteration of the solution. The schematic diagram in Figure 1 outlines the way this information is used to evaluate the contact function. We first compute the minimum distance between a point, $\boldsymbol{x}$, on the P^{th} grain and all other grains as

$$d(\boldsymbol{x}) = \min_{q \neq P} dist(\boldsymbol{x}, \Gamma_q), \tag{7}$$

where $dist(\boldsymbol{x}, \Gamma_q)$ is the minimum Euclidean distance between a point $\boldsymbol{x}$ and an interface Γ_q. The contact function, $\chi(\boldsymbol{x})$, is given by

$$\chi(\boldsymbol{x}) = \begin{cases} 1 & \text{if } d(\boldsymbol{x}) < \delta \\ 0 & \text{otherwise} \end{cases}. \tag{8}$$

If the distance is less than a prescribed threshold δ, we consider the P^{th} grain to be in contact with another grain at the point $\boldsymbol{x}$ on the boundary.

Once the contact function is evaluated on the surface of each grain, we calculate the contiguity tensor ψ_{ij}

$$\psi_{ij} = \frac{1}{L} \int_{\Gamma_P} \chi(\boldsymbol{x}) \hat{n}_i(\boldsymbol{x}) \hat{n}_j(\boldsymbol{x}) \, d\Gamma_P \tag{9}$$

where L is the length of Γ_P [*Takei*, 1998] and $\hat{n}_i$ is the unit normal on the grain surface. The trace of the contiguity tensor, ψ, is also numerically evaluated at each time step for each grain. The anisotropy of the contiguity tensor is then measure by ψ_1/ψ_2 where ψ_1 and ψ_2 are the smallest and largest eigenvalue values of ψ_{ij}, respectively. By this definition, $\psi_1/\psi_2 = 1$ when the tensor is isotropic and decreases as the anisotropy in the tensor increases.

2.3. Calculation of Shear Wave Speed and Anisotropy

In a deforming, partially molten aggregate, anisotropy is produced by (a) deformation of individual grains along dominant slip planes and (b) redistribution of melt into an anisotropic geometry. Deformation of crystals along specific slip planes and the resultant Lattice Preferred Orientation (LPO) can exert significant influence in the anisotropy of the structure. While the general technique, outlined below is able to address both sources of anisotropic texture, in this work, we assume that the viscosity of the grains remain constant, leading to a Newtonian rheology. In crystals, such behavior is achieved by deformation in the diffusion creep regime. In this regime, slip of dislocations and generation of an LPO is suppressed. Consequently, in our analysis, following the works of *Takei* [1998] and *Takei* [2005], we assume that the anisotropy is caused only by the anisotropic distribution of melt geometry. The work of *Holtzman and Kendall* [2010] outlines the competition between these two effects.

Consider an initially isotropic partially molten aggregate in the x–y plane. As this aggregate is deformed, the components of the contiguity tensor change, leading to a change in the shear wave speed, based on the direction of polarization. For example, the shear wave traveling in the z direction while vibrating along the i^{th} direction in the x–y plane will experience a reduction in shear wave speed, δV_{Si}, given by

$$\frac{\delta V_{Si}}{V_{Si}^{eq}} = \frac{\delta \psi_{ii}}{2\psi} \frac{S_{zizi}^{eq} - S_{zizi}^{s}}{S_{zizi}^{eq}}, i = x, y \tag{10}$$

where ψ_{ii} is the component of the contiguity tensor on the face perpendicular to the i axis, ψ is the trace of the contiguity tensor, V_{Si}^{eq} is the shear wave speed in the undeformed aggregate, and S_{ijkl} is the elastic compliance tensor. Assuming the both the solid (superscript $m = s$) and the undeformed, partially molten matrix (superscript $m = eq$) are isotropic, the compliance tensors are defined as [*Takei*, 1998]

$$S_{ijkl}^{m} = \frac{1}{9k_m}\delta_{ij}\delta_{kl} + \frac{1}{4\mu_m}\left[\delta_{ik}\delta_{jl} + \delta_{il}\delta_{jk} - \frac{2}{3}\delta_{ij}\delta_{kl}\right], \tag{11}$$

where δ_{ij} is the Kronecker delta, k_m is the bulk modulus, and μ_m is the shear modulus. For the solid matrix, k_s and μ_s simply represent the temperature, pressure, and composition dependent bulk and shear moduli. For the partially molten matrix, the effective compliance tensor, S_{ijkl}^{eq}, is sensitive to the interconnection between the load bearing grains through the contiguity in the undeformed state. Using this definition of the compliance tensor, we can show that the last term on the right-hand side of equation (10) becomes

$$\frac{S_{zizi}^{eq} - S_{zizi}^{s}}{S_{zizi}^{eq}} = 1 - \frac{\mu_{eq}}{\mu_s}. \tag{12}$$

Following the parameterization of *Takei* [2002], we can express the quantity on the right-hand side of equation (12) as

$$1 - \frac{\mu_{eq}}{\mu_s} = (1 - \psi)^n, \tag{13}$$

where the exponent n is also a function of the trace of contiguity ψ. Combining equations (10) to (13), we find the simplified relation for the variations in the seismic wave speed as

$$\delta V_{Si} = V_{Si}^{eq}\left[\frac{\delta\psi_{ii}}{2\psi}\right](1 - \psi)^n, \tag{14}$$

where $i = x, y$. The quantity within square brackets on the right-hand side of equation (14) represent the contribution of anisotropic contiguity in shear wave splitting. If the contiguity is the same as the undeformed or equilibrium stage, $\delta\psi_{ii} = 0$, leading to $\delta V_{Si} = 0$. In this analysis, we assume that $V_{zx}^{eq} = V_{Si}^{eq} = V_0(\phi, \psi)$, where ϕ is the melt volume fraction. This formulation directly relates anisotropy in the microstructure, $\delta\psi_{ii}$, to the anisotropy in shear wave speed δV_{Si}. Using the formulation of *Takei* [2002], we can calculate $V_0(\phi, \psi)$ for a known melt fraction and contiguity. In our numerical experiments, we calculated the scalar contiguity, ψ, and four components of the contiguity tensor ψ_{ij}, for all grains at each time step. In the absence of deformation, the shear wave speed through the partially molten aggregate at a given depth is controlled by the elastic properties of the solid and melt, the potential temperature, and the bulk solid composition. In the equilibrium assemblage, the influence of melt on the shear wave speed is controlled by the melt geometry and the volume fraction.

We use the numerical model MuMaP [*Hier-Majumder et al.*, 2014] to create vertical profiles of shear wave speed. The elastic properties of the reference mantle were obtained from the work of *Xu et al.* [2008], for mantle potential temperatures of 1300 K and 1500 K, for a basalt fraction of 0.2 in the bulk composition. We used the equation of state for 5% carbonated peridotite from *Ghosh et al.* [2007] to obtain the physical properties of the melt phase. Next, we insert an approximately 45 km thick partially molten zone in the reference mantle. The top of the temperature sensitive partially molten zone was set at depths of 60 km for a potential temperature of 1500 K and 70 km for the potential temperature of 1300 K. These depths roughly correspond to the intersection of 40 and 80 Ma old oceanic geotherms with CO_2-H_2O rich peridotite solidus of *Wallace and Green* [1988]. We then calculated the reduction in shear wave speed when the melt is distributed in tubules in an undeformed state for melt volume fractions of 0.001 and 0.02, for dihedral angles of 5° and 25°, respectively. The detailed method of these calculations have been outlined in *Hier-Majumder et al.* [2014]. To test the role of deformation in the shear wave reduction, we also calculated the relative reduction in shear wave speed caused by melt films. Following the equations of *Walsh* [1969], we carried out these calculations for a melt volume fraction of 0.001 and film aspect ratios of 0.002 and 0.005.

3. Development of Anisotropy

In this section, we present the results for the development of anisotropy in contiguity for both pure and simple shear deformation. We also present the results for seismic anisotropy for the pure shear case.

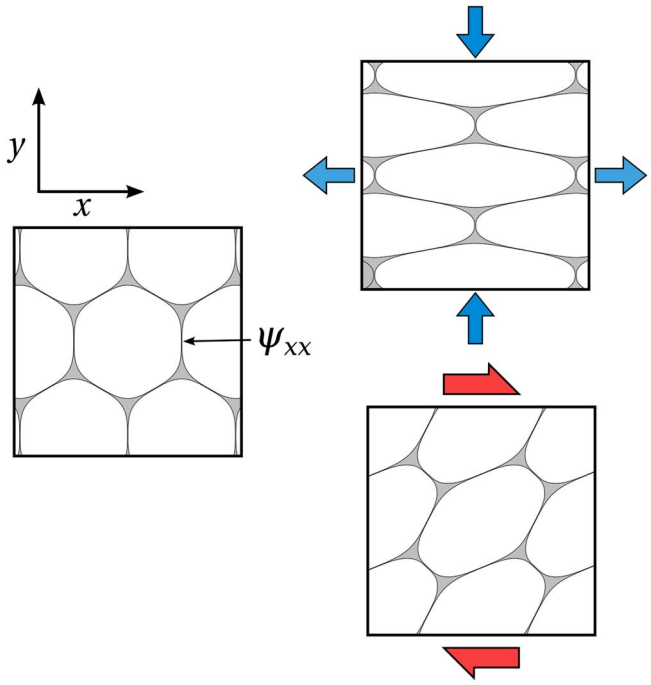

Figure 2. Microstructure of a small section from the deforming aggregate. On the left, the undeformed aggregate is shown. The ψ_{xx} component of the contiguity tensor is illustrated on a grain boundary of the undeformed aggregate. On the right microstructures resulting from (top) pure shear and (bottom) simple shear deformation are shown.

3.1. Development of Anisotropic Contiguity

During the course of deformation in the numerical experiments, as the grain shapes evolved, so did the anisotropy in the contiguity. The synthetic microstructures in Figure 2 depicts the change in the shape of grains during pure and simple shear deformation. In the undeformed state, the melt is distributed evenly along tubules in three grain junctions. After pure shear deformation, the intergranular contact along the boundaries perpendicular to the *x* axis is substantially reduced, as the pockets on each end nearly touch each other, effectively transitioning into a film-like texture. An important consequence of this transformation is a significant reduction of the ψ_{xx} component of contiguity. In the simple shear experiment, we also see the development of such film like structures along grain boundaries oriented in a sense antithetic to the applied, dextral shear.

As the partially molten aggregate is deformed in pure shear, the ψ_{xx} component of contiguity tensor decreases while ψ_{yy} increases. The magnitude of contiguity, ψ, remains nearly constant. Data in Figure 3a demonstrate this trend. In the absence of deformation (zero strain), both diagonal components of contiguity are equal. The sum of these two components are the same as the total contiguity, ψ, which is the trace of the contiguity tensor. Each data point in the plot represents an average made over 1200 grains in the aggregate. As the aggregate is compressed parallel to the *y* axis, grain boundaries parallel to the direction of compression open up. Consequently, ψ_{xx}, the component of contiguity on the face perpendicular to the *x* axis, decreases. The opposite is observed for the faces normal to the *y* axis, resulting in an increase in the value of the ψ_{yy} component. This behavior of the aggregate is qualitatively similar to the change in microstructure observed in fractured, porous rocks [*Mavko et al.*, 2003]. The trace of the contiguity tensor, ψ, remains nearly constant during deformation. The shaded region in the plot depicts the range of values of contiguity measured by *Takei* [2005] in her samples deformed in pure shear. As the plot indicates, the trace of our contiguity matches the experimental measurements well.

During pure shear deformation, the anisotropy becomes stronger but no rotation of the contiguity tensor is observed. In Figure 3b, the ratio between the *xx* and *yy* components of the contiguity tensor are plotted with the ratio between the two eigenvalues, ψ_1 and ψ_2. Both sets of data indicate a reduction in the ratio, signaling a strengthening of the anisotropy, while the data sets become indistinguishable as strain increases. As the principal axes of the applied strain rate remain stationary, this behavior of anisotropy development is physically reasonable. This observation qualitatively matches well with the experimental observation of *Takei* [2005] and *Daines and Kohlstedt* [1997].

During simple shear deformation, variations in the ψ_{xx} and ψ_{yy} components are comparatively small. In Figure 4a, initially the ψ_{xx} component is slightly larger than the ψ_{yy} component. As deformation proceeds, however, the ψ_{xx} component is modestly reduced in magnitude. Similar to the pure shear case, the contiguity ψ remains nearly constant and consistent with the experimentally observed contiguity of *Takei* [2005]. The difference in behavior between the two types of deformation is explained by the data in Figure 4b. Unlike the pure shear case, the ratio between the principal components differs significantly from the ratio between the *x* and *y* components. This difference arises from the rotational nature of the simple shear flow.

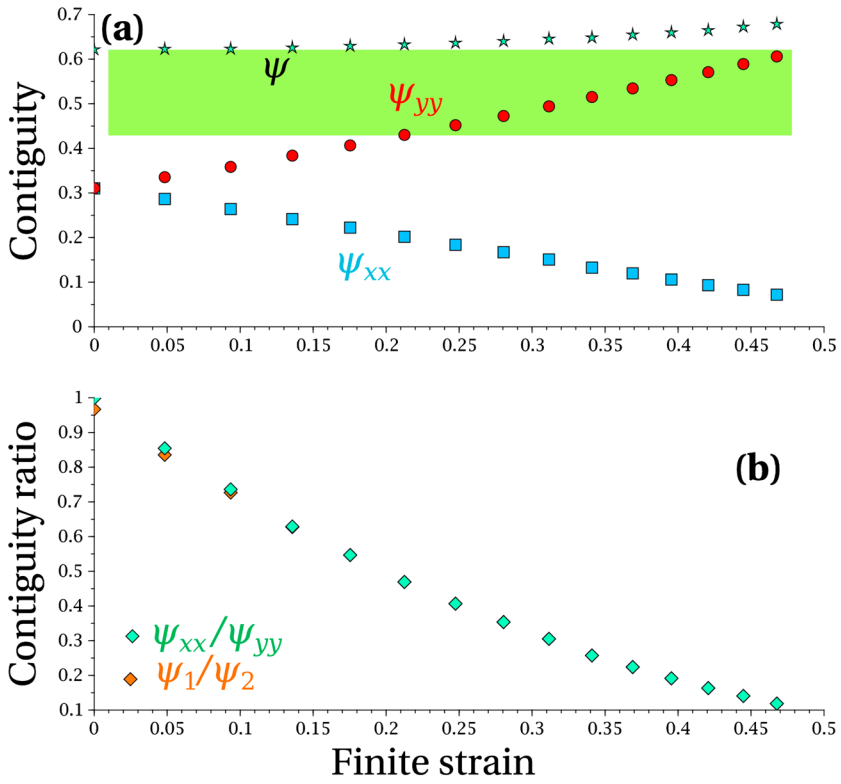

Figure 3. Development of anisotropic contiguity in pure shear. (a) Plot of the magnitude of contiguity, ψ, and the components ψ_{xx} and ψ_{yy} as a function of shortening. Each data point is averaged over 1200 grains in the numerical experiment. Width of the shaded region represents the range of contiguity reported by *Takei* [2005] for comparable melt volume fractions. (b) Ratio between the two principal components of contiguity (ψ_1/ψ_2) and the ratio between the ψ_{xx} and ψ_{yy} components. The data sets are practically indistinguishable and overlie each other.

As the grains deform, they undergo rotational motion, leading to a rotation of the contiguity tensor. As a result, the contiguity tensor is as anisotropic as the pure shear case, but the principal axes of anisotropy differ from the coordinate axes. It should be noted that the shear strains in our numerical experiments are relatively modest in comparison with experimental measurements [*King et al.*, 2011; *Hustoft and Kohlstedt*, 2006; *Hier-Majumder and Kohlstedt*, 2006], whereas the strain in the numerical pure shear experiments are substantially higher than experimental measurements such as *Daines and Kohlstedt* [1997].

3.2. Development of Seismic Anisotropy

In the two dimensional aggregate, melt is confined in pockets along the junction of three grains only. Due to the hexagonal symmetry of the grains, all components of contiguity are equal. Consequently, the speed of shear waves traveling through this aggregate is independent of either the direction of propagation or the directions of polarization. As deformation of the aggregate forces melt out of the triple grain junctions and wets a larger fraction of two grain contacts or grain boundaries, however, the speed of shear waves vary based on the direction of propagation and the direction of polarization. For the present two-dimensional case, we present the results for a shear wave traveling out of the plane, in the *z* direction.

During pure shear, $\delta V_{Sx}/V_0$ decreases while $\delta V_{Sy}/V_0$ increases, as depicted in the plots in Figures 5a and 5b. The rate of decrease of $\delta V_{Sx}/V_0$ slows down significantly, achieving a steady-state around a finite strain of 0.4. At this strain, the changes in the ratio $\delta V_{Sy}/V_0$ also slow down sharply. This trend is explained by the development of well-wetted vertical grain boundaries. Both changes reach approximately 1.5% by the steady-state. In Figure 5c, we plot the total anisotropy $(V_{sx} - V_{Sy})/V_0$ as a function of strain. Following the trend of each component, the total anisotropy also attains a nearly constant value of −0.03 at a shortening of 0.4. We overlay the data with a polynomial fit in Figures 5a and 5b. The fitting function and coefficients are listed in Table 1.

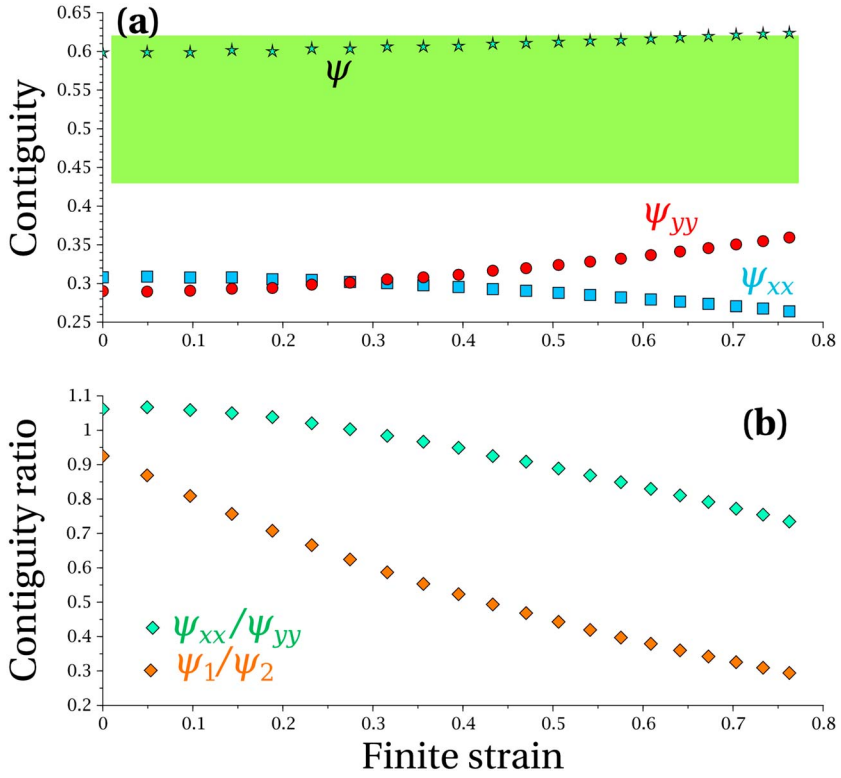

Figure 4. Development of anisotropic contiguity during simple shear. Each data point is averaged over 900 grains in the numerical experiment. (a) Plots of magnitude of contiguity ψ, and the components ψ_{xx} and ψ_{yy} as a function of shear strain. Width of the shaded region represents the range of contiguity reported by *Takei* [2005] for comparable melt volume fractions. (b) Ratio of the two principal components of contiguity (ψ_1/ψ_2) and the ratio between the ψ_{xx} and ψ_{yy} components.

During simple shear, however, reduction of the shear wave speeds with *x* polarization and increase of those with *y* polarization is less than the pure shear. Up to a shear strain of 0.8, δV_{Sx} is reduced by 0.4%, while δV_{Sy} increases by 0.6%, leading to a total anisotropy of approximately 1% as show in Figures 6a–6c. Since the principal components of the anisotropy tensor rotate away from the *x* and *y* plane, the shear wave anisotropy along the coordinate axes is weaker in this case.

Development of well wetted grain boundaries are manifested in the seismic signature of the partially molten region. In the following section, we discuss the implications for this textural change on the seismic signature of the LAB.

4. Discussion

4.1. Implications of the Numerical Experiments

As deformation forces melt to wet greater fraction of grain boundaries, shear wave splitting will become more prominent. The cartoons in Figures 7a and 7b demonstrate the way seismic anisotropy from our numerical experiments can be mapped to the natural conditions. In our numerical experiments, contiguity is reduced along planes perpendicular to the *x* axis, rendering $\psi_{xx} < \psi_{yy}$. This situation is akin to the experimental observations of increase in aspect ratio of melt pockets in the direction of maximum compressive stress by *Daines and Kohlstedt* [1997]. Thus, we have $V_{Sy} > V_{Sx}$. If we consider two simple end member cases as outlined in Figure 7b, predominantly horizontal grain boundary wetting will lead to $V_{SH} > V_{SV}$. If the grain boundary wetting is vertical, however, the opposite effect will take place. Although we do not consider the role of LPO in the matrix, this picture is qualitatively similar to the predictions by *Holtzman and Kendall* [2010]. It is important to note that in neither set of numerical experiments we observed formation of large melt-rich bands. The shear wave anisotropy is brought about by grain scale redistribution of melt.

The results from our two-dimensional calculations are suitable for understanding the nature of observed seismic anisotropy arising from variations in wave speed associated with different polarization directions on

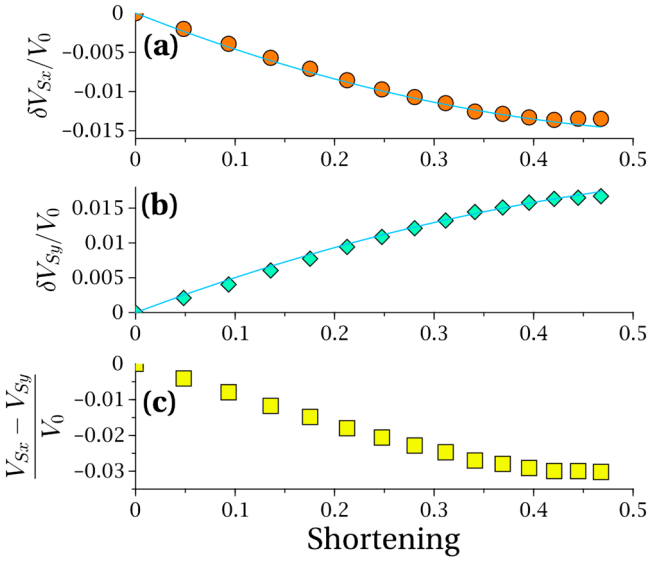

Figure 5. Development of shear wave anisotropy as a function of strain in pure shear. Variations in the wave speed of a wave traveling out of the plane of deformation with a polarization parallel to the(a) *x* axis, δV_{Sx}, and (b) *y* axis, δV_{Sy}, normalized by the wave speed in the isotropic aggregate, V_{eq}. The blue lines are polynomial fits to the data. Parameters for the fit and the fitting function are reported in Table 1. (c) Total seismic anisotropy, difference between the two polarizations of the shear wave, normalized by V_{eq}. The strain on the horizontal axis is shortening. Each data point represent an average of the 1200 grains.

a plane. As our results indicate, the primary impact of deformation is the formation of two-dimensional melt films, adequately captured by the current model. While the two-dimensional model allows us to evaluate the seismic implications for the two end member cases presented in Figure 7b, future three-dimensional models of deformation will be helpful to evaluate the seismic implications for more complex styles of deformation such as torsion.

4.2. Limitations and Future Directions

While our results are qualitatively similar to previous experimental studies of *Daines and Kohlstedt* [1997] and *Takei* [2005], direct quantitative comparison of the results is less straightforward. In their experimental study of melt topology in deformed peridotites, *Daines and Kohlstedt* [1997] presented microstructural measurements of melt pocket aspect ratio but provided no measurement of contiguity. In the analog material experiment of shear wave speed reduction during deformation, *Takei* [2005] present the anisotropy of shear wave speed, but the anisotropy of contiguity was not measured in the experimental samples. The work of *Takei* [2005] also reports a small reduction in the trace of the contiguity tensor, ψ, during deformation. As our results in Figures 3a and 4a indicate, this quantity shows very small variations during deformation in our simulations. The width of the shaded box in these figures indicates, however, the magnitude of scalar contiguity from our simulations are still quite similar to the magnitude of scalar contiguity measured by *Takei* [2005]. To address some of these discrepancies, future measurements of three-dimensional anisotropic contiguity from both deformed experimental samples and numerical models will be useful. While our results of anisotropy in shear wave speed matches the seismic observations quite well, some caution needs to be exercised in calculating shear wave speed reduction using our results.

The two major seismic constraints on the nature of the LAB arise from the shear wave anisotropy and shear wave speed reduction. In the following section, we take a microstructure-based approach to provide a model for the nature of the LAB and the G discontinuity. We use the results from this work to estimate the shear wave anisotropy in the LAB. To calculate the reduction in shear wave speed, we use two different models for the deformed and undeformed states.

Table 1. Parameters for Fit to the Reduction in Shear Wave Speed $\delta V_{Si}(i = x, y)$ as a Function of Strain in From Pure and Simple Shear Experiments[a]

Experiment	Quantity	p_1	p_2
Pure shear	δV_{Sy}	0.054	−0.036
	δV_{Sx}	−0.050	0.041
Simple shear	δV_{Sy}	0.002	0.008
	δV_{Sx}	−0.001	−0.006

[a]The equation for the fit is $\delta V_{Si} = p_1\epsilon + p_2\epsilon^2$, where ϵ is either shortening or the shear strain.

In our numerical simulations, the trace of the contiguity tensor, ψ, remains nearly unaffected by deformation. As a result, using ψ as the only parameter, as in the poroelastic model of *Takei* [1998], for measuring shear wave reduction would lead to the conclusion that deformation has little influence on the reduction of shear wave speed. This poroelastic model is based on the assumption that the grains are undeformed and the contiguity is isotropic. As a result, we considered this model unsuitable for calculating shear wave speed reduction

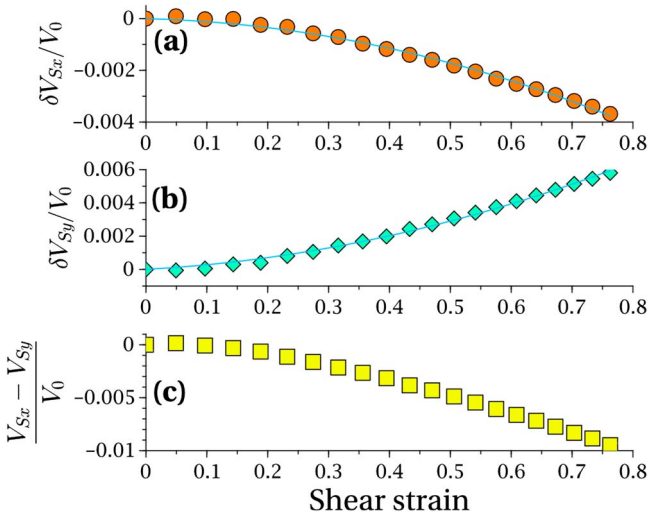

Figure 6. Development of shear wave anisotropy as a function of strain in simple shear. Variations in the wave speed of a wave traveling out of the plane of deformation with a polarization parallel to the(a) *x* axis, δV_{Sx}, and (b) *y* axis, δV_{Sy}, normalized by the wave speed in the isotropic aggregate, V_{eq}. The blue lines are polynomial fits to the data. Parameters for the fit and the fitting function are reported in Table 1. (c) Total seismic anisotropy, difference between the two polarizations of the shear wave, normalized by V_{eq}. The strain on the horizontal axis is the shear strain. Each data point represent an average of the 900 grains.

in the strongly anisotropic microstructure developed by deformation. For undeformed aggregates with melt residing in tubules, however, this model is suitable, and we use this model to predict shear wave reduction by melt tubules. Future, anisotropic contiguity-based poroelastic models will help alleviate this issue.

Due to the complication mentioned above, we chose the classic model of *Walsh* [1969] to calculate the shear wave speed reduction caused by melt films. The shear wave reduction predicted by this model relies on the aspect ratio and volume fraction of melt films. While it is difficult to constrain the aspect ratio of the melt films, the melt volume fraction can be constrained from petrology [*Wallace and Green*, 1988; *Sifré et al.*, 2014]. Noticing that the shear wave speed reduction using the model of *Walsh* [1969] is strongly dependent on the unconstrained value of film aspect ratio, we use a range of aspect ratios for which petrologically relevant melt fractions can cause shear wave reduction similar to the observed values. With these caveats, in the following section we present an argument for incipient melting induced seismic signature of the LAB.

4.3. Implications for the G Discontinuity and LAB

Recent seismological observations reveal a complex relationship between seismic anisotropy and shear wave speed reduction beneath the lithosphere [*Schmerr*, 2012; *Beghein et al.*, 2014; *Nettles and Dziewoński*, 2008]. The work of *Schmerr* [2012] observe nearly 5% reduction in the shear wave speed underneath the Pacific. The second observation involves 4% anisotropy of globally averaged shear wave speed beneath the LAB [*Nettles and Dziewoński*, 2008]. Finally, the work of *Beghein et al.* [2014] demonstrate that the G discontinuity, which was often considered to coincide with the LAB, arises from a distinct signature of seismic anisotropy. For the relatively young oceanic lithosphere, both the G discontinuity and the LAB occur at the same depth.

An independent set of constraints arise from magnetotelluric observations of the LAB and laboratory measurements of electrical conductivity of carbonate-rich melts. A nearly horizontal channel of elevated electrical conductivity is revealed by magnetotelluric studies of the LAB [*Evans et al.*, 2005; *Naif et al.*, 2013]. Recent laboratory measurement of electrical conductivity of $CO_2 - H_2O$ bearing silicate melts by *Sifré et al.* [2014] indicate that incipient melting (<1 vol % melting) of a volatile-fluxed asthenosphere can explain this observed elevated electrical conductivity. Such incipient melting is aided by flattening of the solidus of $CO_2 - H_2O$ bearing peridotites [*Wallace and Green*, 1988]. In this section, we present a model that aims to explain the observed shear wave speed reduction and anisotropy due to horizontally aligned incipient melt films and proposes a mechanism for a possible separation between the G discontinuity and the LAB for older oceanic lithospheres.

The plots in Figure 8 outline the key observations from seismic anisotropy and melting. The profiles in Figures 8a and 8b based on the model BYSX14 [*Beghein et al.*, 2014] represent the profiles of shear wave velocity and seismic anisotropy from two regions in that study. The profiles marked "young" and "old" are averaged over geographic regions bounded between ±5° latitude and −49° longitude and ±5° latitude and 165° longitudes, respectively. In Figure 8b, the G discontinuity is marked by a transition from $V_{SH} < V_{SV}$ to $V_{SH} > V_{SV}$ over a relatively narrow depth range of 70-80 km. The plot on Figure 8c plots the solidus of

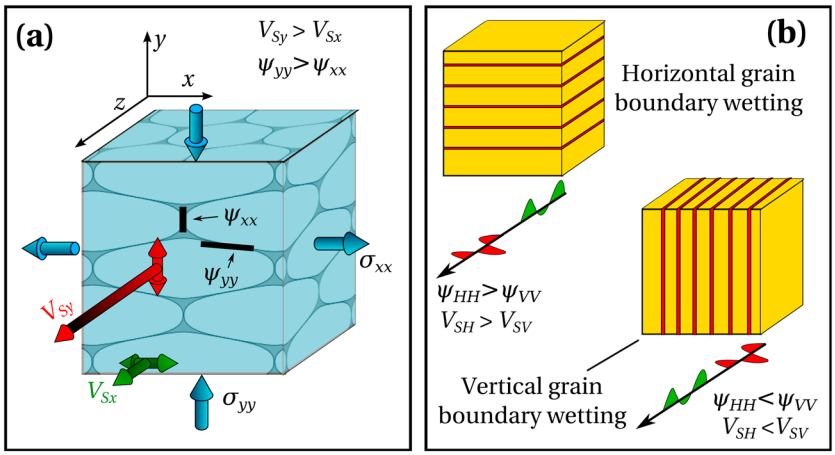

Figure 7. (a) A cartoon identifying the components of anisotropy and stress in an aggregate deformed by pure shear. Also shown are two waves V_{Sx} and V_{Sy}, that travel out of the plane of deformation and are polarized in the x and y directions, respectively. The component of contiguity, ψ_{xx}, is reduced by predominant wetting of the grain boundaries perpendicular to the x direction. (b) Two illustrative cases resulting from preferential wetting of either horizontal or vertical grain boundaries. When the grain boundary melt films are horizontal, $V_{SH} > V_{SV}$, while the picture is reversed for vertical melt films.

$CO_2 - H_2O$ bearing peridotites for the same depth range [*Wallace and Green*, 1988]. Also overlain on the solidus are oceanic geotherms based on the half-space cooling model (thick lines) and plate cooling model (thin lines) for 40 Ma and 80 Ma old oceanic lithspheres, respectively. Irrespective of the two cooling models, the geotherms intersect the solidus within the observed depth range of the G discontinuity. The inflection of the solidus at around 70 km depth is caused by a subsolidus reaction of orthopyroxene + dolomite → clinopyroxene + olivine + vapor, forcing melting to occur at a nearly constant depth for both warm and cold

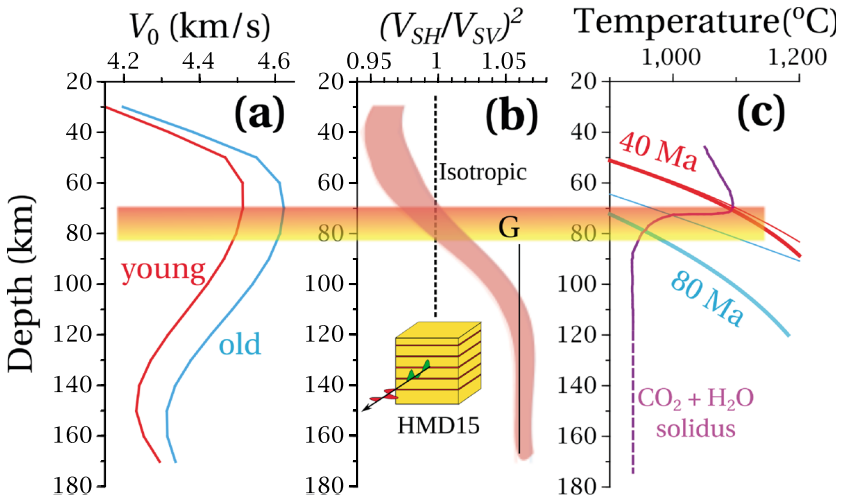

Figure 8. Vertical profiles of (a)shear wave velocity and (b) shear wave anisotropy from model BYSX14 *Beghein et al.* [2014]. The width of the profile in Figure 8b represents the range of regional variations. The cartoon illustrates the nature of shear wave anisotropy generated by the formation of horizontally oriented melt films caused by grain boundary wetting. The solid vertical line, marked HMD15, indicates the steady state shear wave anisotropy from the pure shear simulations in Figure 5c. (c) Thermal structure and melting relation for volatile-induced incipient melting beneath the oceanic lithosphere. The purple curve represents the $CO_2 - H_2O$ saturated peridotite solidus from *Wallace and Green* [1988]. The solid line represent the experimental P-T conditions used in determining the solidus, while the broken segment is an extrapolation of the curve to higher pressures. The red and blue geotherms correspond to 40 and 80 Ma old oceanic lithospheres, respectively. The thin curves were calculated using the plate cooling model for an average plate thickness of 100 km, thermal diffusivity of 1×10^{-6} ms^{-2}, and a mantle temperature of 1300°C [*Turcotte and Schubert*, 2001, Section 4.17]. The thick curves represent oceanic geotherms calculated using the half space cooling model [*Turcotte and Schubert*, 2001, Section 4.16] using the same parameters. The horizontal bar, annotated G, marks our interpretation of the top of the Gutenberg discontinuity.

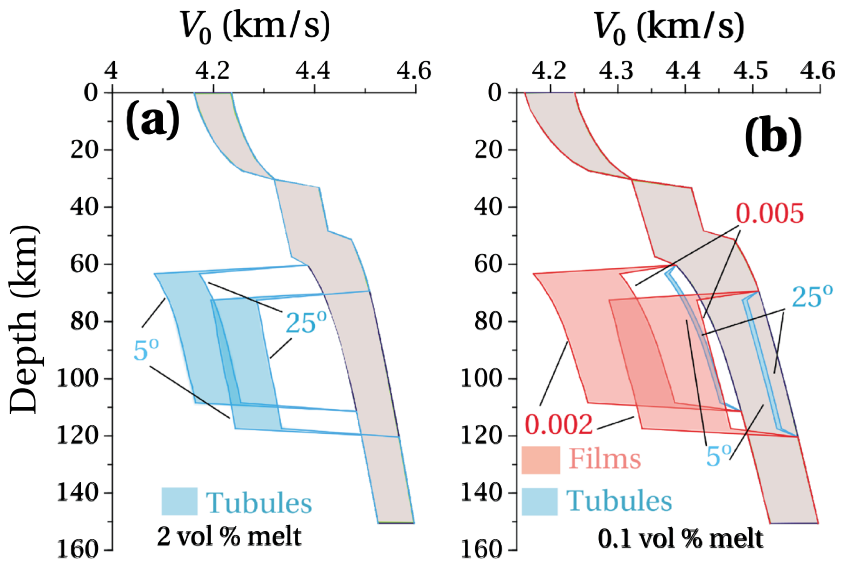

Figure 9. Effect of melt geometry in shear wave speed reduction in the LAB. (a) The gray shaded region represents shear wave speed profiles varying between potential temperatures of 1300 K and 1500 K, from *Xu et al.* [2008]. The temperature sensitive top and the bottom of the melting zones are marked by broken horizontal lines. The blue shaded profiles represent shear wave speed reduction caused by 2 vol % melt in tubules for dihedral angles of 5° and 25°. (b) The thin blue curves correspond to reduction in the shear wave speed of the reference mantle if the 0.1 vol % melt is distributed in grain boundary tubules. The red regions represent reduction in the shear wave velocity if the same volume fraction of melt is distributed in thin grain boundary films. The width of the region represents the variations in the aspect ratio of the film. For the melt fraction of 0.1 vol %, the observed 5% reduction in shear wave velocity can be explained by melt films of aspect ratio 0.002, created by deformation.

plates. Based on the inflection of the solidus and the laboratory measurements of electrical conductivity, *Sifré et al.* [2014] concluded that the electric signature of the LAB can be explained by < 1 vol % melt in thin films. In Figure 9, we explore the resultant seismic signature of such incipient melting.

We consider two shear wave speed profiles for a reference mantle at temperatures of 1300 K and 1500 K, as depicted in Figures 9a and 9b. For the warmer mantle, we place the top of the melting zone at 60 km, while we place the top of the melting zone at 70 km for the cooler mantle. The seismic profiles in Figure 9a compares the reduction of shear wave speed due to melt in tubules of dihedral angles varying between 5° and 25°. As the profiles indicate, reduction of the dihedral angle, for the same volume fraction of melt, causes a sharp reduction in the shear wave speed. Based on this profile, the observed 5% reduction in shear wave speed can be explained by 2 vol % melt in tubules with a dihedral angle of 5°.

Although the shear wave speed reduction can be explained by 2 vol % melt in tubules, several other factors need to be taken into consideration. The isotropic distribution of melt in this case fails to explain the observed anisotropy in seismic and magnetotelluric signatures of the LAB. If partially molten, it is not possible to generate anisotropy by LPO of crystals by deformation while keeping the melt in uniformly distributed tubules. In addition, the permeability of 2 vol % melt may be sufficiently large to allow gravitational rise of the lighter melt rendering the source region depleted in melt. It is illustrative, therefore, to predict the seismic signature of a smaller volume fraction of melt distributed in films.

The profile in Figure 9b compares the reduction in shear wave speed caused by 0.1 vol % melt in films and tubules. At such small volume fractions, variations in the dihedral angle produce very small variations in the shear wave speed reductions, as indicated by the width of the blue profiles in this figure. We also plot the shear wave speed reduction by melt distributed along grain boundary films of aspect ratio varying between 0.002 and 0.005 using the relations from *Walsh* [1969]. When the melt is distributed in films of aspect ratio 0.002, the shear wave speed can be reduced to 5% despite the small melt volume fraction.

The schematic diagram in Figure 10 summarizes our interpretation of the seismic signature of the G discontinuity and the LAB. The flat $CO_2 - H_2O$ rich peridotite solidus triggers incipient melting at depths of 60-70 km for a large part of the oceanic plate. Aided by the strong shearing associated with plate motion,

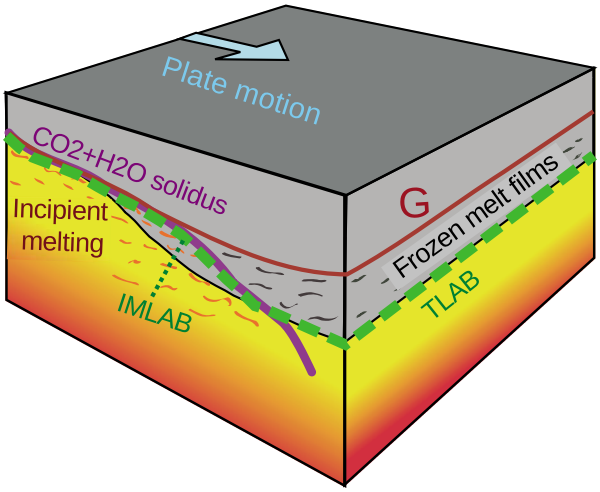

Figure 10. A schematic diagram outlining the nature of volatile induced incipient melting and the consequences for the Gutenberg discontinuity and the LAB. The purple curve is $CO_2 - H_2O$ enriched peridotite solidus. The black line marks the LAB, while the dark red line marks the Gutenberg discontinuity. In the younger lithosphere, incipient melting along the solidus reduces the shear wave speed and introduces seismic anisotropy. As the LAB follows the incipient melting curve, it is annotated as IMLAB. The sharp drop in the solidus for older lithospheres, freezes the incipient melt lenses in place. The LAB for this older lithosphere is thermal in nature and annotated as TLAB in the diagram.

the melt films are aligned horizontally, rendering $V_{SH} > V_{SV}$. In this region, the LAB and G discontinuity both follow the volatile-bearing peridotite melting curve. Since the LAB is controlled by incipient melting, we designate this section of the LAB as IMLAB. For oceanic crusts older than ~120 Ma, the temperature falls below the solidus. The films of partial melt are frozen into amphibole and carbonate bearing lenses. While the shape-preferred orientation of the lenses render the aggregate anisotropic, they are not as effective in reducing the shear wave speed. In these older oceanic lithosphere, the LAB, which is now dominated by elevated temperature appears at a greater depth than the G discontinuity.

Seismic anisotropy induced by small volume fraction of melt in horizontal films, agrees well with the suggestion of *Kawakatsu et al.* [2009]. The relatively large volume fraction of melt in tubules required to explain the seismic anisotropy poses two problems. First, such a large volume fraction of melt will likely be gravitationally unstable. The small volume fraction of melt in films is more likely to be retained at the source region as the low permeability and high surface tension at such small melt fractions will prevent efficient extraction of the melt [*Hier-Majumder*, 2011; *Hier-Majumder and Courtier*, 2011; *Hier-Majumder et al.*, 2006]. Secondly, the presence of small amounts of carbon will lead to small degree of incipient melting in the LAB [*Sifré et al.*, 2014]. While this observation may explain the global radial anisotropy of shear wave, regional trends of $V_{SH} < V_{SV}$ can be likely attributed to the regional geodynamic set up [*Holtzman and Kendall*, 2010]. In addition, horizontal melt films help explaining the observed nearly horizontal region of elevated electrical conductivity.

5. Conclusions

In this article, we demonstrate that the anisotropy in contiguity increases in a strongly nonlinear fashion with progressive pure and simple shear deformation. During pure shear deformation, the anisotropy in shear wave speed also increases in a strongly nonlinear fashion and achieves a steady state during our numerical experiments. Our results demonstrate that the observed seismic anisotropy in the LAB can be explained by formation of such films in nearly horizontal alignment.

Acknowledgments
The work in this paper has been supported by an NSF grant EAR 1215800. In compliance with the AGU data policy, the data required to produce the results of this paper can be requested from the corresponding author by formal written communication. We thank Caroline Beghein for sharing the data from the seismic model BYSX14. The manuscript greatly benefited from insightful reviews by two anonymous reviewers and several discussions with Nick Schmerr.

References

Beghein, C., K. Yuan, N. Schmerr, and Z. Xing (2014), Changes in seismic anisotropy shed light on the nature of the Gutenberg discontinuity, *Science*, *343*, 1237–1240.
Daines, M. J., and D. L. Kohlstedt (1997), Influence of deformation in melt topology in peridotites, *J. Geophys. Res.*, *102*, 10,257–10,271.
Drombosky, T., and S. Hier-Majumder (2015), Development of anisotropic contiguity in deforming partially molten aggregates: 1. Theory and fast multipole boundary elements method, *J. Geophys. Res. Solid Earth*, *120*, 744–763, doi:10.1002/2014JB011068.
Evans, R. L., G. Hirth, K. Baba, D. Forsyth, A. Chave, and R. Mackie (2005), Geophysical evidence from the MELT area for compositional controls on oceanic plates, *Nature*, *437*, 249–252.
Fischer, K. M., H. A. Ford, D. L. Abt, and C. A. Rychert (2010), The lithosphere-asthenosphere boundary, *Annu. Rev. Earth Planet. Sci.*, *38*, 551–575.
Ghosh, S., E. Ohtani, K. Litasov, A. Suzuki, and T. Sakamaki (2007), Stability of carbonated magmas at the base of the Earth's upper mantle, *Geophys. Res. Lett.*, *34*, L22312, doi:10.1029/2007GL031349.
Hier-Majumder, S. (2008), Influence of contiguity on seismic velocities of partially molten aggregates, *J. Geophys. Res.*, *113*, B12205, doi:10.1029/2008JB005662.
Hier-Majumder, S. (2011), Development of anisotropic mobility during two-phase flow, *Geophys. J. Int.*, *186*, 59–68.

Hier-Majumder, S., and A. Courtier (2011), Seismic signature of small melt fraction atop the transition zone, *Earth Planet. Sci. Lett.*, *308*, 334–342.
Hier-Majumder, S., and D. Kohlstedt (2006), Role of dynamic grain boundary wetting in fluid circulation beneath volcanic arcs, *Geophys. Res. Lett.*, *33*, L08305, doi:10.1029/2006GL025716.
Hier-Majumder, S., Y. Ricard, and D. Bercovici (2006), Role of grain boundaries in magma migration and storage, *Earth Planet. Sci. Lett.*, *248*, 735–749.
Hier-Majumder, S., E. Keel, and A. Courtier (2014), The influence of temperature, bulk composition, and melting on the seismic signature of the low velocity layer above the transition zone, *J. Geophys. Res. Solid Earth*, *119*, 971–983, doi:10.1002/2013JB010314.
Holtzman, B. K., and J.-M. Kendall (2010), Organized melt, seismic anisotropy, and plate boundary lubrication, *Geochem. Geophys. Geosyst.*, *11*, Q0AB06, doi:10.1029/2010GC003296.
Hustoft, J., and D. Kohlstedt (2006), Metal silicate segregation in deforming dunitic rocks, *Geochem. Geophys. Geosyst.*, *7*, Q02001, doi:10.1029/2005GC001048.
Kawakatsu, H., P. Kumar, Y. Takei, M. Shinohara, T. Kanazawa, E. Araki, and K. Suyehiro (2009), Seismic evidence for sharp boundaries of oceanic plates, *Science*, *324*(5926), 499–502.
Kim, S., and S. J. Karilla (2005), *Microhydrodynamics: Principles and Selected Applications,* chap. 13, Dover, Mineola, N. Y.
King, D. S. H., S. Hier-Majumder, and D. L. Kohlstedt (2011), An experimental study of the effects of surface tension in homogenizing perturbations in melt fraction, *Earth Planet. Sci. Lett.*, *307*, 735–749.
Leal, G. (1992), *Laminar Flow and Convective Transport Processes*, Butterworth-Heinemann, Stoneham, Mass.
Manga, M., and H. Stone (1993), Buoyancy-driven interactions between two deformable viscous drops, *J. Fluid Mech.*, *256*, 647–683.
Mavko, G., T. Mukerji, and J. Dvorkin (2003), *Rock Physics Handbook*, Cambridge Univ. Press, Cambridge.
Naif, S., K. Key, S. Constable, and R. L. Evans (2013), Melt-rich channel observed at the lithosphere-asthenosphere boundary, *Nature*, *495*, 356–359.
Nettles, M., and A. M. Dziewoński (2008), Radially anisotropic shear velocity structure of the upper mantle globally and beneath North America, *J. Geophys. Res.*, *113*, B02303, doi:10.1029/2006JB004819.
Pozrikidis, C. (2001), Interfacial dynamics for stokes flow, *J. Comput. Phys.*, *169*, 250–301.
Rychert, C. a., P. M. Shearer, and K. M. Fischer (2010), Scattered wave imaging of the lithosphere-asthenosphere boundary, *Lithos*, *120*, 173–185.
Schmerr, N. (2012), The Gutenberg discontinuity: Melt at the lithosphere-asthenosphere boundary, *Science*, *335*, 1480–1483.
Sifré, D., E. Gardés, M. Massuyeau, L. Hashim, S. Hier-Majumder, and F. Gaillard (2014), Electrical conductivity during incipient melting in the oceanic low-velocity zone, *Nature*, *509*(7498), 81–85, doi:10.1038/nature13245.
Takei, Y. (1998), Constitutive mechanical relations of solid-liquid composites in terms of grain boundary contiguity, *J. Geophys. Res.*, *103*, 18,183–18,203.
Takei, Y. (2002), Effect of pore geometry on v_p/v_s: From equilibriium geometry to crack, *J. Geophys. Res.*, *107*(B2), ECV 6-1–ECV 6-12, doi:10.1029/2001JB000522.
Takei, Y. (2005), Deformation induced grain boundary wetting and its effect on accoustic and rheological properties of partially molten rock analogue, *J. Geophys. Res.*, *110*, B12203, doi:10.1029/2005JB003801.
Turcotte, D., and G. Schubert (2001), *Geodynamics*, John Wiley, New York.
Wallace, M. H., and D. H. Green (1988), An experimental determination of primary carbonatite magma composition, *Nature*, *335*, 343–346.
Walsh, J. (1969), New analysis of attenuation in partially melted rock, *J. Geophys. Res.*, *74*, 4333–4337.
Xu, W., C. Lithgow-Bertolini, L. Stixrude, and J. Ritsema (2008), The effect of bulk composition and temperature on mantle seismic structure, *Earth Planet. Sci. Lett.*, *275*, 70–79.